The Astrophysical Journal, 492:L83–L93, 1998 January 10

THE ON-ORBIT PERFORMANCE OF THE SPACE TELESCOPE IMAGING SPECTROGRAPH

R. A. Kimble,[1] B. E. Woodgate,[1] C. W. Bowers,[1] S. B. Kraemer,[1,2] M. E. Kaiser,[1,3] T. R. Gull,[1] S. R. Heap,[1]
A. C. Danks,[4] A. Boggess,[2,5] R. F. Green,[6] J. B. Hutchings,[7] E. B. Jenkins,[8] C. L. Joseph,[9] J. L. Linsky,[10]
S. P. Maran,[11] H. W. Moos,[3] F. Roesler,[12] J. G. Timothy,[13] and D. E. Weistrop[14]
STIS Investigation Definition Team
J. F. Grady, J. J. Loiacono, L. W. Brown, M. D. Brumfield, D. A. Content, L. D. Feinberg, M. N. Isaacs, C. A. Krebs,
V. L. Krueger, R. W. Melcher, F. J. Rebar, H. D. Vitagliano,[15] and J. J. Yagelowich
NASA Goddard Space Flight Center, Greenbelt, MD 20771
W. W. Meyer, D. F. Hood, V. S. Argabright, S. I. Becker, M. Bottema,[15] R. R. Breyer, R. L. Bybee, P. R. Christon,
A. W. Delamere, D. A. Dorn, S. Downey, P. A. Driggers, D. C. Ebbets, J. S. Gallegos, H. Garner,
J. C. Hetlinger, R. L. Lettieri, C. W. Ludtke, D. Michika, R. Nyquist, D. M. Rose, R. B. Stocker,
J. F. Sullivan, C. N. Van Houten, and R. A. Woodruff
Ball Aerospace and Technologies Corporation, Boulder, CO 80306
S. A. Baum, G. F. Hartig, V. Balzano, C. Biagetti, J. C. Blades, R. C. Bohlin, M. Clampin, R. Doxsey,
H. C. Ferguson, P. Goudfrooij, S. J. Hulbert, R. Kutina, and M. McGrath
Space Telescope Science Institute, 3700 San Martin Drive, Baltimore, MD 21218
D. J. Lindler, T. L. Beck, J. K. Feggans, P. C. Plait, and J. L. Sandoval
Advanced Computer Concepts, Inc., NASA Goddard Space Flight Center, Laboratory for Astronomy and Solar Physics, Code 681, Greenbelt, MD 20771
R. S. Hill, N. R. Collins, R. H. Cornett, W. B. Fowler, R. J. Hill, W. B. Landsman,
E. M. Malumuth, and C. Standley
Hughes STX Corporation, NASA Goddard Space Flight Center, Laboratory for Astronomy and Solar Physics, Code 681, Greenbelt, MD 20771
and
M. Blouke,[16] A. Grusczak,[17] R. Reed,[6] R. D. Robinson,[18] J. A. Valenti,[10] and T. Wolfe[6]
Received 1997 August 4; accepted 1997 October 30; 1997 December 30

ABSTRACT

The Space Telescope Imaging Spectrograph (STIS) was successfully installed into the *Hubble Space Telescope* (*HST*) in 1997 February, during the second *HST* servicing mission, STS-82. STIS is a versatile spectrograph, covering the 115–1000 nm wavelength range in a variety of spectroscopic and imaging modes that take advantage of the angular resolution, unobstructed wavelength coverage, and dark sky offered by the *HST*. In the months since launch, a number of performance tests and calibrations have been carried out and are continuing. These tests demonstrate that the instrument is performing very well. We present here a synopsis of the results to date.

Subject headings: instrumentation: spectrographs — space vehicles — techniques: spectroscopic — ultraviolet: general

1. INTRODUCTION

The Space Telescope Imaging Spectrograph (STIS) is a second-generation spectrograph for the *Hubble Space Telescope* (*HST*), designed to replace and greatly expand on the capabilities of two highly successful first-generation instruments, the Goddard High-Resolution Spectrograph (GHRS) and the Faint Object Spectrograph (FOS). Both of these were removed during the STS-82 servicing mission to permit the installation of STIS, into the axial instrument bay formerly occupied by GHRS, and the Near-Infrared Camera and Multiobject Spectrograph (NICMOS) (Thompson et al. 1998), into the FOS bay.

The principal advances offered by STIS stem primarily from the use of large format, two-dimensional array detectors. Two photon-counting Multianode Microchannel Array (MAMA) detectors (each read out in a 2048 × 2048 format) record UV light, and one 1024 × 1024 pixel CCD covers the visible. Compared with the 1 × 512 linear array Digicon detectors em-

[1] NASA Goddard Space Flight Center, Laboratory for Astronomy and Solar Physics, Code 681, Greenbelt, MD 20771; kimble@stars.gsfc.nasa.gov.
[2] Catholic University of America, Department of Physics, Washington, DC 20064.
[3] Johns Hopkins University, Department of Physics and Astronomy, 34th and Charles Street, Bloomberg Center, Baltimore, MD 21218-2695.
[4] Hughes STX Corporation, NASA Goddard Space Flight Center, Laboratory for Astronomy and Solar Physics, Code 681, Greenbelt, MD 20771.
[5] 2420 Balsam Drive, Boulder, CO 80304.
[6] National Optical Astronomy Observatories, P.O. Box 26732, 950 North Cherry Avenue, Tucson, AZ 85726-6732.
[7] Dominion Astrophysical Observatory, Herzberg Institute of Astrophysics, National Research Council of Canada, 5071 West Saanich Road, RR. 5, Victoria, British Columbia V8X 4M6, Canada.
[8] Princeton University Observatory, Peyton Hall, Princeton, NJ 08544-1001.
[9] Rutgers University, Department of Physics and Astronomy, P.O. Box 849, Piscataway, NJ 08855-0849.
[10] JILA, Campus Box 440, University of Colorado, Boulder, CO 80309-0440.
[11] NASA Goddard Space Flight Center, Space Sciences Directorate, Code 600, Greenbelt, MD 20771.
[12] University of Wisconsin at Madison, Department of Physics, 2531 Sterling Hall, Madison, WI 53706.
[13] Centre for Research in Earth and Space Science, York University, North York, Ontario M3J 1P3, Canada.
[14] University of Nevada, Physics Department, 4505 Maryland Parkway, Las Vegas, NV 89154-4002.
[15] Deceased.
[16] Scientific Imaging Technologies, Inc., P.O. Box 569, Beaverton, OR 97075.
[17] Hughes Danbury Optical Systems, Inc., 100 Wooster Heights Road, Danbury, CT 06810.
[18] Computer Sciences Corporation, NASA Goddard Space Flight Center, Laboratory for Astronomy and Solar Physics, Code 680, Greenbelt, MD 20771.

ployed by the first-generation *HST* spectrographs, these two-dimensional array detectors enable STIS to provide observing modes with large spatial and/or spectral multiplexing gains.

For spectroscopic observations, STIS brings the following new capabilities to *HST*:

1. Long-slit and slitless imaging spectroscopy over the full 115–1000 nm range, at *HST* angular resolution over 25″–50″ fields of view.
2. Medium- and high-resolution echelle spectroscopy in the ultraviolet, with 20–35 times greater simultaneous wavelength coverage than in corresponding GHRS modes.
3. Higher spectral resolution in the 115–310 nm range than that available with any previous space instrument.
4. Higher throughput to longer visible/near-IR wavelengths than the FOS (whose photocathode response extended to ∼700 nm).
5. Much lower dark rate per resolution element in the far-ultraviolet than the first-generation spectrographs, permitting spectroscopy of fainter sources.
6. Coronagraphic spectroscopy, utilizing the excellent image contrast of the *HST*.

All three STIS detectors can be used for imaging observations as well. Although the available filter complement is limited (especially in the visible), STIS imaging provides the following powerful capabilities:

1. Solar-blind imaging at high sensitivity, using low-noise photon counting detectors with more than 20 times higher throughput than the Wide Field Planetary Camera 2 (WFPC2) when using its visible-blocking Woods filters.
2. Higher sensitivity broadband visible imaging than WFPC2, resulting from very wide bandpasses feeding a higher quantum efficiency CCD with lower read noise.
3. Superior coronagraphic capability compared with previous *HST* instruments.

A number of Early Release Observations have been made for the purpose of demonstrating these new *HST* capabilities. This issue presents examples of STIS long-slit and slitless imaging spectroscopy of galactic nuclei and SN 1987A (Bower et al. 1998; Hutchings et al. 1998; Sonneborn et al. 1998), medium- and high-resolution UV echelle spectroscopy of stars and the interstellar medium (Heap et al. 1998; Jenkins et al. 1998; Walborn et al. 1998), visible/near-IR spectroscopy of a brown dwarf near a much brighter companion (Schultz et al. 1998), deep CCD imaging of a gamma-ray burst transient (Pian et al. 1998) and of gravitational lens arclets (Sahu et al. 1998), and the serendipitous detection of a high-redshift galaxy in parallel observing (Gardner et al. 1998).

An active Servicing Mission Orbital Verification (SMOV) program began shortly after launch and has recently concluded. The report given here is a snapshot of the on-orbit performance results obtained to date. For critical parameters that have not yet been or cannot be measured directly on orbit, we also cite relevant results from the preflight calibration.

Additional characterization and calibration of STIS performance will be carried out in the *HST* cycle 7 calibration program that is just beginning. Results will be reported in future publications and in documentation developed and maintained by the Space Telescope Science Institute (STScI), such as the STIS Instrument Handbook (Baum et al. 1996), Advisories, and Instrument Science Reports. These can be examined using the STScI STIS web site.

2. OVERVIEW OF STIS

STIS was built by Ball Aerospace for the Laboratory for Astronomy and Solar Physics at NASA Goddard Space Flight Center (GSFC), under the direction of the principal investigator, B. Woodgate of GSFC. In this section, we highlight the principal design features and observing modes of STIS as background for the discussion to follow. More detailed descriptions of the design, optical diagrams, and detector schematics are given by Woodgate et al. (1992, 1998), Danks et al. (1996), and in the STScI STIS Instrument Handbook (Baum et al. 1996); this last provides a comprehensive guide to STIS characteristics and operations for the general observer.

Light entering the instrument is first corrected for *HST*'s spherical aberration and for the astigmatism at the STIS field point by a two-element corrector system within the instrument, analogous to the corrector pairs deployed by COSTAR during the first *HST* servicing mission (the COSTAR mirrors that fed GHRS were retracted prior to the installation of STIS into the GHRS bay). The STIS corrector system (a concave sphere and an anamorphic asphere) produces a well-focused image at the entrance slit wheel of the spectrograph, where one of 65 slits or apertures can be selected. These consist of clear slits of assorted widths and lengths for long-slit and echelle spectroscopy, ND-filtered slits for calibration and bright-object spectroscopy, filtered and unfiltered apertures for imaging, as well as coronagraphic slits and apertures with occulting wedges and bars. Alternate light paths can also illuminate the slit plane with the output of various line and continuum lamps for wavelength calibration, flat-fielding, and target acquisition.

After passing through the slit wheel, light is collimated by a mirror and directed to the Mode Select Mechanism (grating wheel), where one of 21 gratings, mirrors, or a prism can be positioned in the beam. Order sorters are mounted in front of the gratings where required. The mechanism can also tip/tilt the optic in use to select the desired wavelength range for those modes in which the dispersed spectrum overfills the detector format.

The choice of slit, grating wheel element, and tip/tilt angle (specified by designating a desired central wavelength) completely defines the optical configuration. From the grating wheel, the light travels to the appropriate detector either directly or via a fold flat and camera mirror, or via an echelle grating and camera mirror. Shutter and blocker mechanisms are configured as required to keep light out of the instrument during slit and grating wheel motions, to start and stop CCD exposures, and to control stray light cross talk between the various optical paths.

The observing modes of STIS can be divided into four spectral bands. Band 1 (115–170 nm) is covered by a photon-counting MAMA detector, designated the far-ultraviolet (FUV) MAMA, with an opaque CsI photocathode deposited directly on the front of its single curved-channel microchannel plate (C-plate). Band 2 (165–310 nm) is covered by a similar detector, the near-ultraviolet (NUV) MAMA, utilizing a semi-transparent CsTe photocathode on the inside of the detector window. This detector provides additional coverage down to 115 nm in imaging and prism modes, and it serves as a backup to the FUV MAMA. The MAMAs were developed by Ball Aerospace and are both permanently sealed tubes with MgF_2 entrance windows (see Timothy 1994 and Joseph et al. 1995 for further details about the MAMA design and performance). Each MAMA detector incorporates a 1024 × 1024 element anode array, but the processing electronics centroid event po-

TABLE 1
SPECTRAL FORMAT AND RESOLVING POWER FOR STIS PRIMARY SPECTROSCOPIC MODES

Mode Name	Detector	Nominal λ Range (Å)	Å per Exposure	Exposures (Full Band)	Å per Pixel[a]	Resolving Power λ/Δλ (FWHM)	Slit Used (arcsec)	Data Source (Resolving Power)
G140L	FUV MAMA	1150–1700	597	1	0.583	950–1400	52 × 0.050	FLIGHT
G230L	NUV MAMA	1650–3100	1583	1	1.55	500–960	52 × 0.050	FLIGHT
G230LB	CCD	1672–3077	1405	1	1.37	700–1050	52 × 0.100	FLIGHT
G430L	CCD	3050–5550	2809	1	2.75	500–980	52 × 0.100	FLIGHT
G750L	CCD	5500–10000[b]	4993	1[b]	4.88	560–760	52 × 0.100	FLIGHT
PRISM	NUV MAMA	1150–3100	>1950	1	0.47–48[c]	1200–31[c]	52 × 0.050	GROUND
G140M	FUV MAMA	1150–1700	54.3	11	0.0530	7800–19200	52 × 0.050	FLIGHT
G230M	NUV MAMA	1650–3100	89.2	18	0.0872	8200–20600	52 × 0.050	FLIGHT
G230MB	CCD	1650–3100	154	12	0.151	5200–11200	52 × 0.100	FLIGHT
G430M	CCD	3050–5550	283	10	0.277	4900–10100	52 × 0.100	FLIGHT
G750M	CCD	5500–10000	567	9	0.555	5100–10400	52 × 0.100	FLIGHT
E140M	FUV MAMA	1150–1700	587	1[d]	λ/91700	46000	0.200 × 0.060	FLIGHT
E230M	NUV MAMA	1650–3100	808	2	λ/60000	29900–32200	0.200 × 0.060	FLIGHT
E140H	FUV MAMA	1150–1700	202	3	λ/228000	99300–114000[e]	0.200 × 0.090	FLIGHT
E230H	NUV MAMA	1650–3100	277	6	λ/228000	92300–110900[e]	0.200 × 0.090	FLIGHT

[a] For MAMA modes, "pixel" refers to a low-resolution pixel, i.e., the 1024 × 1024 readout format.
[b] A second grating setting can be selected to extend the coverage past the 10600 Å cutoff of the CCD.
[c] The resolution and Å per pixel are specified at 1200 and 3100 Å, respectively.
[d] A second grating setting can be selected to fill in very small gaps between the longest wavelength orders.
[e] Even higher resolution is achievable using narrower slits.

sitions to half the spacing of the anode array, providing improved image sampling and higher resolution (but with larger flat-field variations) in a 2048 × 2048 image format (Kasle & Morgan 1991). For historical reasons, this is referred to as the high-resolution readout mode; all generic references to MAMA pixels in this Letter (and in most other STIS documentation) refer instead to low-resolution pixels in the 1024 × 1024 format.

Bands 3 and 4 (305–555 and 550–1000 nm, respectively) are covered by a backside-thinned, UV-enhanced, multipinned-phase, 1024 × 1024 pixel CCD developed by Scientific Imaging Technologies (SITe). The CCD covers bands 3 and 4 as its prime operating range and provides backup to the NUV MAMA in the 180–305 nm range. The CCD is cooled to an operating temperature of −83°C using a four-stage thermoelectric cooler (TEC). The CCD and TEC are enclosed within a sealed, evacuated housing, whose fused silica window is only slightly cooler than the rest of the instrument, minimizing the condensation of contaminants that could otherwise be deposited directly onto the much colder CCD (see Kimble et al. 1994 for a more comprehensive discussion of the CCD subsystem).

The spectral formats and resolving powers of the primary STIS spectroscopic modes are summarized in Table 1. Long-slit imaging spectroscopy at low and medium resolution is available in all four spectral bands; at low resolution, each spectral band is covered in one exposure. The prism can be used to obtain a complete UV spectrum (115–310 nm) in one exposure, although with widely varying dispersion over that wavelength range. The CCD modes covering band 2 (G230LB and G230MB), originally implemented to provide a backup capability, are designated as prime observing modes because their throughput is higher than that of the corresponding MAMA modes in the longer wavelength portion of the band. Medium- and high-resolution spectroscopy in echelle formats are provided in the two UV MAMA bands only.

Plate scales in the MAMA modes range from 0″.0244 to 0″.0290 per MAMA pixel in the cross-dispersion direction, yielding fields of view of 25″–30″ for imaging spectroscopy. Plate scales in all CCD modes are close to 0″.050 per CCD pixel, yielding a 50″ field of view. The higher dispersion modes (particularly E140H and E230H) have significant demagnification in the dispersion direction (because of the unequal angles of incidence and reflection on the gratings), permitting 2 pixel resolution to be obtained with slightly wider slits that transmit more light. Order separation in the echelle modes ranges from 0″.4 to 1″.8; nevertheless, longer slits can be used to good effect on extended emission-line sources.

Table 2 summarizes the properties of additional calibration

TABLE 2
SPECTRAL FORMAT AND RESOLVING POWER FOR STIS CROSS-DISPERSED AND BACKUP MODES

Mode Name	Detector	Nominal λ Range (Å)	Å per Exposure	Exposures (Full Band)	Å per Pixel[a]	Resolving Power λ/Δλ (FWHM)	Slit Used (arcsec)	Data Source (Resolving Power)
X140M	FUV MAMA	1150–1700	614	1	0.600	870–1680	0.050 × 29	GROUND
X140H	FUV MAMA	1150–1700	200	3	0.195	2500–4500	0.050 × 29	GROUND
X230M	NUV MAMA	1650–3100	827	2	0.808	990–1930	0.050 × 29	GROUND
X230H	NUV MAMA	1650–3100	276	6	0.270	2900–5500	0.050 × 29	GROUND
G140LB	NUV MAMA	1150–1700	621	1	0.606	840–1220	52 × 0.050	DESIGN
G140MB	NUV MAMA	1150–1700	54.8	11	0.0535	9400–14000	52 × 0.050	DESIGN
E140MB[b]	NUV MAMA	1150–1700	620	1	λ/60000	26400	0.200 × 0.060	DESIGN
E140HB[b]	NUV MAMA	1150–1700	202	3	λ/228000	101000	0.200 × 0.090	DESIGN

[a] For MAMA modes, "pixel" refers to a low-resolution pixel, i.e., the 1024 × 1024 readout format.
[b] The backup echelle modes E140MB and E140HB suffer order confusion at the shorter wavelengths.

and backup spectroscopic modes (the latter to be used in the event of detector failure). The first-order "XnnnY" modes in the table use the echelle mode cross-dispersers, tilted to direct the spectrum to the detectors without hitting the echelle gratings. Because their dispersion is orthogonal to that of the primary first-order modes, they could in principle provide greater flexibility for making long-slit observations at specific position angles. The X140H mode also offers an intermediate level of resolution between that of G140L and that of G140M, which would be beneficial for some observations. However, due to the calibration and command development demands of additional modes, and some bright-object protection issues unique to the cross-dispersed modes, these are not supported by STScI for use at this time.

As noted above, STIS also includes imaging modes for all detectors, both for target acquisition and for scientific use. A small number of filters are available, principally in the UV. For the MAMA camera modes, the plate scale is 0."0244 pixel^{-1} over a field of view of 24."7 × 24."7. On the CCD, the plate scale of 0."050 pixel^{-1} yields a field of view of 50″ × 50″ for unfiltered imaging and 28″ × 50″ when using one of the visible filters.

STIS incorporates a number of features to provide fault tolerance and continued functionality in the event of potential component failures. These features (such as redundant control microprocessors and power supplies, dual motor windings, dual drives for critical shutter mechanisms, multiple signal processing chains for the CCD, etc.) are described in more detail by Woodgate et al. (1998). At this writing (after 8 months in orbit), all STIS components are fully functional; the instrument is operating entirely on its primary systems.

3. OPTICAL PERFORMANCE

Focus and alignment.—The focus and alignment process for STIS can be separated conceptually into two principal tasks. First, the various modes must be properly focused from the slit plane to the detectors in order to assure that the specified spectral resolution can be achieved regardless of the spatial structure of the source, through the appropriate choice of slit. Second, the corrector mirror pair must correct and reimage light from the *HST* Optical Telescope Assembly (OTA) to the STIS slit plane, maximizing light concentration at the slit plane and thus optimizing the spectrograph throughput for point sources and spatial resolution for extended sources. Our final criterion for focus and alignment of the corrector mechanism is maximum UV throughput through a 0."100 × 0."090 slit.

Slit-to-detector focus and alignment was established during instrument integration on the ground, and the proper performance of the corrector pair was verified using well-validated *HST* simulators. As discussed below, internal line lamp spectra confirm in flight that the spectroscopic modes have remained focused to the slit plane; small alignment shifts have been taken out by adjusting the tip/tilt of the grating wheel as needed. The crux of on-orbit focus and alignment then is adjusting the focus and tip/tilt of the first STIS corrector mirror to produce the desired performance at the slit plane.

After a sequence of corrector focus sweeps and tip/tilt scans in various modes, final confirmation of optimum slit throughput was obtained using the MAMA detectors in modes G140L and G230L. A comparison of spectra obtained through the 0."100 × 0."090 slit with full, open aperture spectra show that the throughput at the slit plane for this small aperture matches theoretical expectations very closely, with measured values of 39% (121.6 nm), 50% (160 nm), 55% (200 nm), and 60% (270 nm).

A small number of slit transmission measurements have been completed at longer wavelengths in the CCD modes as well. The results have been consistently greater (by 5%–15%) than prelaunch predictions. More slit transmission calibrations are planned during the cycle 7 calibration, particularly for small slits in the UV. It is already clear, however, that the OTA + STIS corrector performance is excellent.

Spectral resolution.—Measurements of the spectral resolution of all STIS primary spectroscopic modes have been made in flight, using an on-board Pt-Cr/Ne line lamp to illuminate the appropriate ∼2 pixels wide slit for each mode, at a similar focal ratio to that delivered by the OTA. The resolutions observed agree closely with similar measurements made during ground calibration and confirm that the nominal requirements have been met.

For the long-slit spectroscopic modes in bands 2, 3, and 4 (165–1000 nm), the resolving power varies by ≤10% over the full field. Only the far-UV (band 1) long-slit modes show significant field dependence. Mode G140L resolving power varies by no more than 10% over ∼75% of the full slit length but degrades at one end of the slit to 70% of the value at field center. Mode G140M shows larger variation, 30% over the central 50% of the slit length. Nevertheless, both modes meet their preflight resolution specifications over more than 70%–75% of the field.

Of particular interest is the ultimate spectroscopic resolution of STIS. Using the narrowest slit, only 0."025 wide in the dispersion direction, we have (in ground calibration) obtained FWHM resolving powers of 134,000–193,000 in echelle mode E140H. On-orbit verification of this capability, including acquisition into this small slit, will be attempted during cycle 7. Even higher resolving power (up to 220,000) was demonstrated on the ground in the E140H mode by turning off the quantum-efficiency–enhancing repeller field in the FUV MAMA detector. This lower throughput, higher resolution configuration of the detector is not currently supported in flight.

Spatial resolution/extraction heights.—Stellar spectra have been obtained in several UV and visible modes in an essentially slitless manner (through the 2″ wide slit). The concentration of light in the cross-dispersion direction has been derived from these spectra; representative results are shown in Figures 1 and 2. The concentration is lowest in the far-UV, where the effects of OTA microripple and STIS internal aberrations are greatest. Optimal spatial concentration is seen in the near-UV (near 300 nm), as expected.

At longer wavelengths, diffraction and, more importantly, point-spread function (PSF) halo effects in the CCD detector spread increasing amounts of light into the wings of the line-spread function. The halo in the CCD develops at wavelengths longer than ∼750 nm, where the CCD silicon begins to become transparent. As an increasing fraction of the incident light reaches the substrate of the backside-illuminated device, scattering in the (unfortunately translucent) substrate material produces an ever larger halo. At the longest wavelengths (1000 nm), the halo extends to hundreds of pixels in radius and contains up to ∼30%–40% of the light, although, of course, each pixel in the halo captures a very small fraction of the peak brightness.

In all CCD modes, at all wavelengths, the FWHM observed in the spatial direction is 2.0–2.2 pixels (0."10–0."11). In the UV, the FWHM ranges from ∼4 pixels (0."10) at 118 nm to ∼3 pixels (0."075) at 160 nm to 2.5 pixels (0."063) at 280 nm.

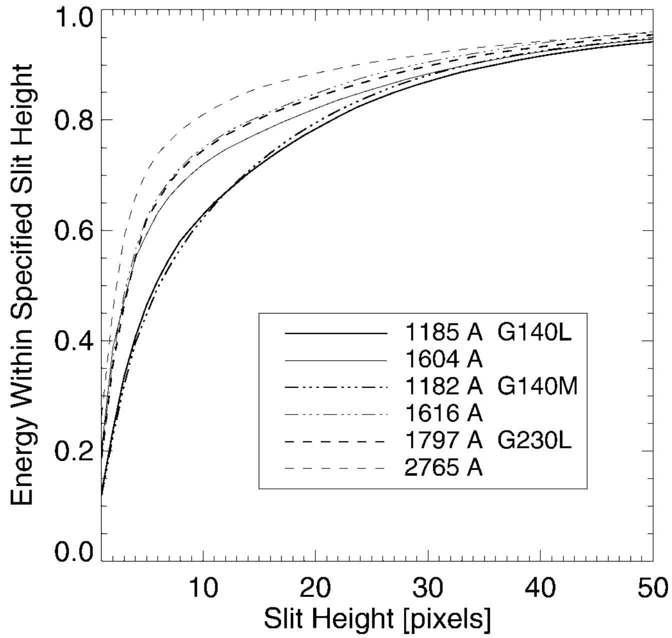

FIG. 1.—Fractional energy vs. extraction slit height for the MAMA detectors (observing through a 2″ wide slit).

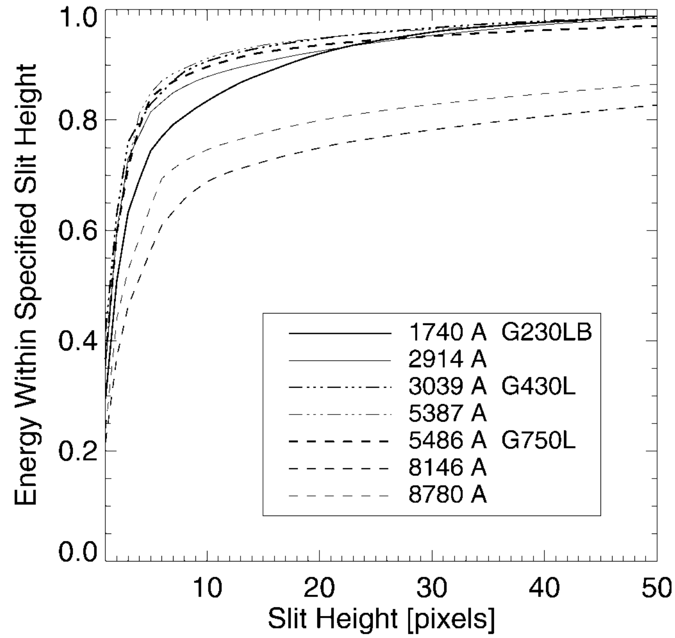

FIG. 2.—Fractional energy vs. extraction slit height for the CCD detector (observing through a 2″ wide slit).

Postobservation processing of spectral data includes extraction of the spectral order(s) and subtraction of background. The optimal extraction height depends on the noise characteristics of the detectors, the particular slit width used, and the scientific purpose of a particular observation. Increasing the extraction height adds more flux, but it also adds read noise and dark current for the CCD and phosphorescent background counts for the NUV MAMA (see § 4). The FUV MAMA has an extremely low intrinsic background, so extending the extraction height will generally increase the signal-to-noise ratio (S/N). However, flux included far from the spectrum has decreasing spectral purity. For measurements of weak absorption features, for example, the increase in total flux will be accompanied by a decrease in the depth of the features. As the slit width is narrowed, light concentration increases, so that a smaller extraction height is necessary to include a fixed percentage of the detected light. The total amount of light detected naturally decreases with smaller slit widths as more light is blocked at the slit.

Standard extraction heights for wide-aperture observations have been selected by STScI, with the goal of including most of the detected light without an excessive amount of detector background, while maintaining spectral purity. An extraction height of 11 pixels was selected for the MAMA modes, and 7 pixels for the CCD modes. Due to the wings of the telescope PSF at the shortest FUV wavelengths and the CCD halo effects at the longest wavelengths, as much as 40% of the detected light is outside the extraction height in the 120 and 1000 nm regions; losses beyond the extraction height are much lower over most of the STIS wavelength range.

Sensitivity.—Absolute calibration of the sensitivity of the OTA + STIS combination began during the SMOV program. All four primary low-dispersion modes (G140L, G230L, G430L, and G750L) have been calibrated, as well as a few specific settings of the echelle modes and the medium-dispersion long-slit modes. All flight calibrations use established *HST* standards (Bohlin, Colina, & Finley 1995; Bohlin 1996), typically white dwarfs, observed through large apertures (the 52″ × 2″ slit). The sensitivity calibrations derived to date are in generally good agreement with preflight predictions based on the ground calibration of STIS and STScI models of the OTA throughput. In-orbit sensitivities and those currently used by the STScI Exposure Time Calculator agree typically to within ∼20%. One notable exception is mode G430L, with sensitivity as much as 60% greater than expected near 330 nm.

There are, however, two spectral regions where the sensitivity is systematically lower than preflight expectations. In the 130–240 nm range, the sensitivity is broadly lower than anticipated. The deviation is largest in the 160–200 nm range, where the sensitivity is about 20%–25% lower than implied by the ground calibration. This trend is seen clearly in modes G140L, G230L, and G230LB. This wavelength region is one in which thin contaminant films frequently produce lower reflection in Al/MgF_2-coated optics such as used in STIS. While repeated measurements before launch show no decline in efficiency in this region, on-orbit monitoring with the CCD mode G230LB shows a marginally detectable throughput decrease of 1% over 2 months at the center of this depression. Monitoring with MAMA modes has not yet had a sufficient time baseline to permit assessment of any trends. Longward of 700 nm, the G750L and G750M sensitivity is lower than early preflight predictions by roughly the amount lost beyond the extraction slit owing to the CCD halo.

Camera-mode image quality.—During SMOV, direct images have been obtained with a variety of detector/filter combinations, permitting a preliminary evaluation of the image quality in these modes. Since some of these images were obtained prior to the final, small corrector adjustments, the final performance may deviate slightly from the results cited here. The CCD detector may be used for imagery with an open aperture, a long-pass filter (>550 nm), or [O III] (501 nm) and [O II] (373 nm) line filters. Open aperture imagery of the globular cluster ω Cen shows 2 × 2 pixel (0″.10 × 0″.10) ensquared energy values of 0.44–0.47 across the 50″ × 50″ field with

TABLE 3
FUV CAMERA IMAGE QUALITY

Filter	λ_0 (nm)	Target	Performance over Field EE (<0″.10)	Reference Value[a] EE (<0″.10)
A25	Clear	NGC 6681	32%–36% over full field	...
F25QTZ	$\lambda > 146$	NGC 6681	39%–43% over full field	46% (155 nm)
F25SRF2	$\lambda > 130$	NGC 6681	33%–39% over full field	43% (145 nm)
F25LYA	122	BPM 16274	27% at field center	38%

[a] Reference values are from Schroeder 1987.

Gaussian fit FWHM values of 1.8–2.0 pixels. Identical values are obtained over the 28″ × 50″ field accepted by the long-pass filter. Images of the white dwarf Feige 34 taken through the [O II] and [O III] filters show 2 × 2 pixel ensquared energy values of 0.50 and 0.47, respectively, at field center.

Because the various modes that are imaged by the MAMA detectors are incident at different angles, the detector surface and focal surfaces are tilted with respect to one another. Therefore, the image quality is expected to be essentially cylindrically symmetric, with the best focus obtained near the field center (parallel to the direction of the long spectroscopic slits), with a degraded performance to either detector edge. This tilt between the detectors and the camera-mode focal planes and the residual astigmatism over the field also make the MAMA camera modes sensitive to *HST* "breathing" (secondary mirror motion due to orbital thermal variations). The differential defocus of the camera fields due to the breathing phenomenon is largest at the edges of the field and smallest at the nominally focused field center. Variations of point-source FWHM values of up to 0″.025 have been measured over an 1800 s observation.

Note, however, that the flux transmitted through a spectrographic slit at field center is much less sensitive to the breathing defocus. Modeling of the telescope PSF suggests that slit transmission variations due to typical breathing amplitudes should be less than 10%–20% for even the smallest STIS slits; the observed count rates versus time for several small-slit STIS observations are in accord with this prediction.

For the FUV camera modes (filtered and unfiltered), Table 3 summarizes the encircled energy (EE) within a 0″.100 diameter and compares it with the performance of an unaberrated OTA, as estimated by Schroeder (1987).

The NUV camera must be used with a filter to provide proper focus. To date, images have been obtained with the bandpass and line filters centered at 182, 191, 270, and 280 nm, but not with the SrF_2 and quartz long-pass filters, which have 128 and 145 nm cutoffs, respectively. The EE performance of the NUV camera is presented in Table 4.

Distortion measurements have also been made for the CCD and FUV camera modes using a series of offset pointings on globular cluster targets. The distortions measured are very small: maximum offsets of 1.1 pixels in the CCD mode (in good agreement with optical ray tracing) and up to 2.75 pixels in the FUV MAMA mode (a combination in this case of optical and microchannel plate distortion).

TABLE 4
NUV CAMERA IMAGE QUALITY

Filter	λ_0 (nm)	Target	Performance over Field EE (<0″.10)	Reference Value[a] EE (<0″.10) (%)
F25CN182	182	NGC 6681	40%–48% over $\frac{2}{3}$ field, 30%–40% over $\frac{1}{3}$ field	55
F25C3	191	LS 749B	41% at a single, off-center field point	57
F25CN270	270	NGC 6681	50%–54% over $\frac{2}{3}$ field, 40%–50% over $\frac{1}{3}$ field	62
F25MG2	280	BPM 16274	51% at field center	63

[a] Reference values are from Schroeder 1987.

Thermal stability.—Thermal stability of the various optical formats has been characterized through thermal vacuum and ambient air ground tests and in orbit. At the time STIS was in final assembly, it was determined that the thermal environment in the *HST* aft shroud would be much warmer than had been specified previously. Since the operating temperatures of the detectors were of concern, the decision was made to remove several insulation blankets and to add heat pipes in order to conduct heat directly from the MAMA detectors to an aft bulkhead radiator plate. A direct result is that the rear portion of the optical bench is not always under positive thermal control, as had been designed originally, but can track external temperature variations due to spacecraft attitude changes.

Fortunately, the thermal time constants are long (∼12 hr), and the deflections produced by typical temperature changes are small. Observations in several STIS modes indicate that thermal drift rates for the optical formats range typically from 0.2 to 0.4 pixels hr^{-1}, corresponding to 10%–20% of a spectral resolution element per hour. Individual exposures are usually less than 2000 s. The automatic wavelength calibration (wavecal) scheduling algorithm generally provides a wavecal within 1 hr of any given science exposure. Additional wavecals can be scheduled by an observer if greater calibration precision is required.

It is important to note that the front end of the STIS instrument, where the corrector and slit wheel are located, *is* under positive thermal control. We therefore do not expect motions within STIS to change the mapping of OTA pointing to STIS slit position. Stability in this region is crucial for keeping targets centered in the small spectroscopic slits.

4. DETECTOR PERFORMANCE

CCD.—Since flight operations of the STIS CCD began, over 4000 images have been taken (bias and dark frames, internal lamp and external target exposures). We highlight key performance characteristics here.

The 1024 × 1024 pixel CCD is a backside-illuminated three-phase device, with 21 μm pixels, multipinned-phase implants and operation, and an enhanced UV response. The backside UV-enhancement process was developed by SITe for the STIS program. The resulting quantum efficiency (QE) (8% at 200 nm, 20% at 300 nm, 44% at 400 nm, 67% [peak] at 610 nm) is stable, does not show QE hysteresis, and does not require a UV flood.

The CCD is fabricated with a readout amplifier in each of the four corners. There is an independent analog signal pro-

TABLE 5
CCD NOISE/DYNAMIC RANGE

Nominal Gain (e DN^{-1})	Measured Gain (e DN^{-1})	Noise (rms) (In-Flight Data)	Linear Range (at 1% roll-off) (e)	Single-Frame Dynamic Range ≡ Linear Range/Noise
1	0.995	4.0 DN = 4.0e	33000	8250
2	2.01	2.7 DN = 5.4e	86000	16000
4	4.11	1.7 DN = 7.0e	144000	20600
8	8.38	1.3 DN = 10.9e	144000	13200

cessing chain for each amplifier, and the STIS flight software supports full-frame, on-chip–binned, or subarray readout with any of the four amplifiers, as well as two and four amplifier readout modes. Initial functional testing on orbit verified that all four amplifier chains were functioning nominally. Observations since that first checkout have been carried out exclusively with the lowest noise amplifier, which was most fully characterized in ground testing. The redundant amplifiers are available as future backups.

Four commandable gain settings are available for the CCD. The noise performance measured in flight and the dynamic range for each setting are summarized in Table 5. Rough gain measurements made in flight are consistent with the more precisely determined ground values shown in the table. Two gain settings are recommended for general use: gain = 1 for the greatest sensitivity on faint targets and gain = 4 for the highest dynamic range and full well.

In-flight mean bias levels vary over roughly 10 DN (data numbers in the 16 bit digitized readout) at gain = 1 and 3 DN at gain = 4 (because of temperature variations in the CCD and processing electronics); however, the *shape* of the bias frames is constant to less than 0.2 DN, so the bias level is well determined by the serial and parallel overscan data read out with each CCD frame. Under a logarithmic stretch, some frames, particularly at gain = 4, show "herringbone" noise that can be discernible to the eye. However, this pattern is of low amplitude, less than 1 DN, and does not significantly affect the overall noise statistics in the image.

Charge transfer efficiency (CTE) was measured by both X-ray and edge response techniques in ground calibration, with parallel CTE results of 0.999994 at 1620e (X-ray), and 0.999991 at 200e and 0.99996 at 10e (edge response). Serial CTEs are higher. The X-ray CTE measurements cannot be duplicated in flight; however, edge response measurements (using the on-board flat-field lamps for illumination) show no significant changes from ground measurements.

The median dark current at the CCD operating temperature of -83°C is only ~0.0015e pixel^{-1} s^{-1}, or 5–6e pixel^{-1} hr^{-1}. Unless significant on-chip binning is employed, the noise from the median dark current is thus negligible compared with the read noise of the system. Of much greater significance are the effects of cosmic rays and radiation-induced hot pixels. With regard to these issues, the performance of the STIS CCD is very similar to that of WFPC2.

The cosmic-ray rate observed on the STIS CCD outside of the South Atlantic Anomaly (SAA) is ~1 event cm^{-2} s^{-1}. Roughly 30–40 pixel s^{-1} are affected at greater than a 20e level. Cosmic rays are most effectively removed from science data by specifying CR-SPLIT exposures to obtain multiple images from which cosmic rays can be vetoed.

As expected for a CCD in space, energetic particle impacts on the STIS CCD produce "hot pixels" with enhanced dark current. As for WFPC2, warming of the CCD by turning off the thermoelectric cooler is effective at "annealing" some portion of the hot pixels. The STIS CCD reaches -5°C with the TEC off; annealing at this temperature for 12 hr is scheduled monthly. The WFPC2 experience suggests that eventually a near steady state is reached in which the number of new hot pixels each month is similar to the number of old hot pixels that "heal" through the annealing process or spontaneously while the CCD is cold; hence, the *net* growth rate of hot pixels over several years on orbit for WFPC2 is less than 8% of the instantaneous growth rate (Biretta et al. 1996). After the first few STIS annealing cycles, the net growth rate of hot pixels is down to about 30% of the instantaneous growth rate; this fraction is expected to decrease as the hot pixel count asymptotically approaches a steady state. CCD dark frames are taken frequently to permit flagging of hot pixels in nearby science exposures. The most effective removal of hot pixels from science data can be accomplished by dithering the pointing between exposures to permit hot pixel vetoing.

The flat-field behavior of the STIS CCD is extremely stable. Short-term (several hour) pixel-to-pixel stability at better than 0.1% rms was verified over several wavelengths spanning the CCD range in ground testing. In flight, broadband flat-field exposures spanning a month constrain any changes in the pixel-to-pixel response to be less than 0.2% rms, and some portion of that variation is attributable to poorly removed hot pixels. Thus, in general, flats constructed using the on-board tungsten continuum lamps provide high S/N rectification of STIS CCD data.

The most significant issue affecting flat-fielding of STIS CCD data is fringing at the longer wavelengths (where the silicon begins to become transparent), caused by interference between the incident beam and the light reflected by the substrate of the backside-illuminated device. The fringing is negligible shortward of ~750 nm but grows to peak-to-peak amplitudes of 25% and 32% at 980 nm for G750L and G750M, respectively.

Rectification of the fringing pattern should be a tractable problem, because the behavior is completely stable with time. However, small shifts in the wavelength mapping onto the detector, caused by grating wheel nonrepeatability and thermal drifts, do cause the fringe pattern to shift from exposure to exposure. Therefore, for accurate fringe removal, it is necessary to take contemporaneous spectral flats using the on-board tungsten lamps (at least until a suitable library of flats can be constructed). Fortunately, the on-board lamps are bright, so the required exposures are short.

The spatial extent of the source along the slit is also an issue in fringe removal. Because of the PSF halo at long wavelengths, an extended source produces a smooth pedestal beneath the fringing modulation that is not present for a point source. However, a judicious combination of short- and long-slit flats should serve. In data taken to date, we have successfully removed the fringes to better than 1% to ~950 nm for a white dwarf spec-

TABLE 6
KEY MAMA PERFORMANCE PARAMETERS

Parameter	FUV MAMA	NUV MAMA
Wavelength range	115–170 nm	165–310 prime, 115–170 backup
Low-resolution pixel size	25 μm × 25 μm	25 μm × 25 μm
Spatial Resolution (FWHM)[a]	22.7 μm	29.3 μm
Quantum efficiency	~21% (142 nm)	~9.5% (237 nm)
Dark rate[b]	(5–10) × 10^{-6} counts pixel^{-1} s^{-1}	(0.6–1.5) × 10^{-3} counts pixel^{-1} s^{-1}
Dynamic Range (10% roll-off):		
Local (MCP limited)[b]	220 counts pixel^{-1} s^{-1}	340 counts pixel^{-1} s^{-1}
Global (electronics limited)	305,000 counts s^{-1}	305,000 counts s^{-1}
Flat-field uniformity (low-resolution pixels[b])	6.4% rms	3.1% rms
Flat-field stability (changes in 2 × 2 pixels[b])	Over 4 months, <1% rms	Over 21 days, <0.68% rms
Visible light rejection (QE at 400 nm)	1.5 × 10^{-10}	2.7 × 10^{-4}

[a] With high-resolution readout.
[b] "Pixel" refers to a low-resolution MAMA pixel here, i.e., the 1024 × 1024 format.

trum using a short-slit flat and for the extended source Io using a long-slit flat. Development of a systematic fringe removal methodology is a key goal of the in-flight calibration program.

Note that STIS imaging is generally unaffected by the fringing, because no narrowband filters are used at long wavelengths, and the sky background is continuum zodiacal light, not airglow emission lines (as on the ground). A broadband continuum input smooths over the fringes completely; only a highly monochromatic, long-wavelength emission-line source would show fringe modulation in imaging mode.

MAMA detectors.—The STIS MAMA detectors began on-orbit operations in late 1997 April. Their use was delayed until software and scheduling changes had been made to deal with an unexpected issue of control electronics resets (see § 5). Since that time, the MAMA detectors have been performing very well (see Fig. 3 [Pl. L4] for examples of MAMA FUV and NUV imaging of the globular cluster NGC 6681, and several of the Early Release Observation papers in this volume for examples of MAMA imaging spectroscopy and echelle spectroscopy).

A few key MAMA performance parameters are shown in Table 6. Most of these data are from ground calibration, except for the dark rate, for which in-flight values are shown. While the detector-only PSF and quantum efficiency cannot be measured directly in flight, the end-to-end STIS performance indicates that the detector resolution and efficiency are nominal.

A positive highlight of the in-flight performance is the extremely low background of the FUV MAMA, 5–10 times lower than the specification. The close agreement of the in-flight dark rate with that seen in ground testing confirms the successful rejection of Cherenkov events produced in the detector window. Cherenkov photons produced by the passage of energetic particles through the detector windows formed the dominant background in the first-generation spectrographs' Digicon detectors; because the multiple Cherenkov photons produced by a particle transit are effectively simultaneous, they are rejected by the MAMA event processing logic.

The only disappointment with the MAMA detectors in flight is the high dark rate of the NUV MAMA. The specified dark rate for the tube was 1.25 × 10^{-4} counts s^{-1} pixel^{-1}, and ground testing led us to expect substantial improvement over that specification in orbit. Unfortunately, in flight, energetic SAA particles excite metastable states in impurities in the window of the NUV MAMA; the subsequent phosphorescent de-excitation of these states produces UV photons that are detected by the MAMA photocathode. This phenomenon has long been recognized, and a screening program for phosphorescence was specifically instituted for the STIS detector windows; however, an error in the ground testing of this particular MgF_2 ingot allowed it to be used despite its poor phosphorescence characteristics.

The observed NUV MAMA background of (0.6–1.5) × 10^{-3} counts s^{-1} pixel^{-1} (the de-excitation rate varies with detector temperature) is roughly an order of magnitude higher than the specification. Over a typical 2000 s single-orbit exposure, the resulting dark count signal in a standard 2 × 11 pixel spectral extraction slit is 26–66 counts. Optimal extraction techniques or the use of a smaller extraction slit reduce the dark contribution below this level. Thus, in short-exposure time observing programs, only very low S/N observations are significantly affected. However, long observations, or those that are binned spectrally or spatially (such as for extended sources), can be significantly compromised by the unwanted background.

The high S/N potential of MAMA observing is a key issue. Intrinsic pixel-to-pixel variations are 3.9% and 2.8% rms for the FUV and NUV MAMA, respectively, in the 1024 × 1024 low-resolution pixel format (which supports the nominal resolution of all STIS modes). Severe odd-even effects in the high-resolution readout lead to much larger rms variations (~45%–50%) in the 2048 × 2048 format. Ground flat fields for both flight MAMA detectors have shown excellent long-term stability, particularly in the low-resolution mode: less than 1.0% rms variations over timescales of weeks to months. The pixel-to-pixel flat-field variations of the NUV MAMA (with the semitransparent photocathode on the window) show little dependence on wavelength or angle of incidence. From ground calibration, we thus have been able to construct superflats at an S/N of greater than 300 per resolution element (2 × 2 low-resolution pixels) that can be applied to all NUV modes (Bohlin, Lindler, & Kaiser 1997). An on-board deuterium continuum lamp will permit construction of new NUV MAMA flats as required.

The flat fields of the FUV MAMA also show little wavelength dependence over most of the bandpass, but they do appear to show some angle of incidence effects. Hence, to construct the highest S/N flat fields for the STIS FUV modes (which come in over a range of incidence angles), individual flats may have to be constructed on orbit for each observing mode, using the krypton continuum lamp in the on-board calibration subsystem.

It is important to recognize, however, that the raw response variations are significantly smoothed by the actual illumination pattern. Convolving the flats with a Gaussian profile of 2 low-resolution pixels FWHM (representative of the cross-dispersion profiles in STIS spectroscopy) reduces the response variations to 2.5% (FUV) and 1.8% (NUV) per low-resolution pixel in the dispersion direction, and to 1.4% (FUV) and 0.92% (NUV) per 2 pixel wide spectral resolution element. The MAMAs should therefore support point-source spectroscopy up to S/N = 70 (FUV) and 110 (NUV) per spectral resolution element *without applying a flat-field calibration at all*.

A preliminary evaluation of the MAMA S/N performance in flight has been performed with very encouraging results. Spectra of the *HST* standard stars GRW +70°5824 and GD 153 have been obtained in modes G230L and G140L, respectively. For both observations, after subtraction of the background, the point-source spectra were extracted using an 11 pixel high extraction slit. Cubic splines were then fitted to 20 resolution element–wide segments of the spectra. The extracted spectra were then divided by these low-frequency approximations, in order to examine the statistical fluctuations in the data.

The results are as follows. For the NUV MAMA, the GRW +70°5824 spectrum has a peak S/N potential (from counting statistics alone) of ~200 per 2 pixel resolution element. The rms values of the observed spectrum divided by the low-frequency approximation, *without using a flat*, correspond to an S/N of ~105 per 2 pixel resolution element, in excellent agreement with the estimate derived above. Carrying out the same analysis after dividing by the high S/N ground flat yields an S/N of ~150 per 2 pixel element. For the FUV MAMA observation of GD 153, the counting statistic limit is an S/N of ~160 near the peak of the spectrum. In this case, the fluctuations seen in the extracted spectrum correspond to an S/N of ~80 *without using a flat* and ~110, after dividing by a ground-based FUV MAMA flat field. The procedure and results are described in more detail by Kaiser, Lindler, & Bohlin (1997).

Even greater smoothing of the response variations occurs when observing in the echelle modes. In this case, the Doppler effects of orbital motion shift the spectrum back and forth over a few high-resolution pixels in modes E140M and E230M, and over as many as ±12 high-resolution pixels in modes E140H and E230H. (Resolution is maintained using real-time Doppler compensation on board or through ground processing of time-tag data; see § 5). With a typical Doppler amplitude of ±8 high-resolution pixels in the high-resolution echelle modes, the rms variations over a 2 pixel resolution element are reduced to ~0.7% (FUV) and ~0.3% (NUV), and even the high-resolution modulations are smoothed to ~5% rms.

As this Letter goes to press, preliminary results have just been reported from a STIS test of the F-P SPLIT technique previously employed to obtain very high S/N data with the first generation *HST* spectrographs. In this technique, multiple spectra of the target are acquired, offset from each other in the dispersion direction, but overlying each other as closely as possible in the cross-dispersion direction. Iterative analysis of the resulting data then permits a simultaneous solution for the source spectrum and the flat-field response of the instrument. A preliminary analysis of MAMA echelle spectra taken in this manner (in modes E140M and E230M) yields S/Ns of greater than 250 per low-resolution pixel in the spectral direction (integrated over the cross-dispersion profile) and greater than 350 per 2 pixel spectral resolution element. Details of the observations and analysis will be presented in an Instrument Science Report (Gilliland et al. 1997) to be posted on the STScI STIS web page.

Thus, between the use of on-board calibration lamps to derive spectral flats, the smoothing effects of the illumination pattern and Doppler shifting, and the F-P SPLIT techniques, the MAMA detectors should routinely achieve the specified S/N performance of greater than 100 per resolution element (when count statistics permit), and the ultimate S/N capability of STIS MAMA observations appears to be well beyond that level.

5. INSTRUMENT OPERATIONS

Detector electronics resets.—The biggest surprise encountered in operating STIS in flight has been the response of the detector control electronics to the radiation environment. Digital communication between the STIS control section microprocessor and the MAMA and CCD control electronics is optically coupled in order to eliminate conducted electrical noise and thereby maintain a low noise environment for the detectors. Unfortunately, the detector reset circuitry has been found to respond to transient spikes on the outputs of the optical isolator components by partially resetting the detectors. These transients can be produced by the passage of trapped SAA particles or cosmic rays through the optical isolators. Although these components had been properly screened for total radiation dose effects, the transient response of the optical-isolator reset-circuit combination was not recognized preflight.

In the CCD subsystem, the partial resets are relatively infrequent (roughly one per month of continuous operation) and are quite benign. A few CCD control voltages are set to nonfunctional but nonharmful values. By scheduling CCD voltage reconfiguration commands at each SAA exit or before CCD observation blocks, the chances of losing data from a CCD reset are rendered negligible.

The MAMA partial resets are both more frequent (approximately one per day per MAMA *if* the MAMA low-voltage power is left on during SAA passages) and more complex. One effect of the partial reset is to turn off the detector high voltage abruptly. Although the detectors can withstand such shutdowns (as they must during the infrequent spacecraft safings), daily shutdowns of this type would be unnecessarily stressful to the high-voltage system. In addition, when the partial reset occurs, there is a small but nonzero probability (1 in ~500) that a high-voltage ramp-up to the full power supply rails can be spuriously commanded; this would very likely damage the MAMA tube if allowed to proceed. Once the reset phenomenon was recognized on orbit, the MAMA low-voltage power was left off until protective software was installed on board. This software monitors the MAMA subsystems on 40 ms timescales and is designed to intercept a reset-induced ramp-up before it can reach hazardous voltage levels.

In order to avoid potential stresses and risks to the MAMA detectors, they are now being operated in the following manner. The MAMA low-voltage system is cycled off for each SAA crossing but is powered on the rest of the time to maintain thermal stability in the instrument. The MAMA high voltage, on the other hand, is ramped up and down at the nominal slow ramp rate once per day, in the block of contiguous non–SAA-crossing orbits, if the MAMA is scheduled for use that day. The MAMAs have been operated under this regimen for approximately 130 days. They have experienced seven resets outside of the SAA in that time. Hence, the best current estimate is that each MAMA will be shut down abruptly by a particle-induced reset approximately every 3 months (since the MAMA high voltage is on less than half of the time), and the spurious voltage ramp-up is unlikely ever to begin.

The principal effect of the resets, therefore, is to lower the available duty cycle for MAMA observations to about 40% of *HST* orbits. During the current period, when NICMOS observations are being accelerated to maximize its scientific yield before its cryogen is depleted, this duty cycle is more than adequate to schedule MAMA science. More complex, higher duty cycle operating schemes may be considered at a later time if required.

Target acquisition.—The STIS flight software has the capability of autonomously acquiring targets and centering them in spectroscopic slits. The process involves using the STIS CCD to take images of the field, including the target, and of a spectroscopic slit, the latter illuminated using one of the STIS Pt-Cr/Ne line calibration lamps. The flight software determines target and slit positions via flux-weighted centroiding and sends requests to the *HST* main computer (the NSSC-1) for slews to correct the pointing.

Two types of autonomous target acquisition have been tested with STIS during SMOV, point-source acquisition and diffuse-source acquisition. The former was demonstrated using an isolated white dwarf, GD 153. The target was positioned in the $0''.2 \times 0''.2$ slit to an accuracy of 0.2–0.5 CCD pixels ($0''.010$–$0''.025$) in both spatial and dispersion directions. The diffuse-source acquisition algorithm is used for extended sources, particularly those without a strong central peak. It was tested using the galaxies M84 and NGC 1399 as targets, with a resulting positional accuracy of ~1–1.5 CCD pixel ($0''.050$–$0''.075$) in each axis. Both accuracies are significantly better than preflight estimates.

An optional second stage of target acquisition for improving the target centering within a slit, termed a “peakup,” has also been tested several times, again using the STIS CCD. In performing a peakup, the flight software executes a scan pattern, taking images at each point. The final pointing is calculated by taking the flux-weighted centroid over the scan pattern. Peakups performed in CCD imaging mode produced centering within the slit to within the limits of measurability, or better than 0.1 CCD pixel. Note that the point-source acquisition accuracies demonstrated above indicate that point-source peakups are required only for slits smaller than $0''.2$ in length or width.

Dispersed light peakups are used for bright targets that would saturate the CCD in the shortest available exposure time if viewed in imaging mode through a clear slit. This capability has been demonstrated successfully as well.

Bright-object protection.—The FUV and NUV MAMAs, like any microchannel plate-based photon counters, require protection from overillumination. Excessive global count rates can potentially damage the tubes, while excessive local exposure can alter the detector flat field, compromising the ability to calibrate exposures at a high S/N level. In order to preserve the health and stability of the MAMA detectors, the predicted global and local brightnesses of potential MAMA targets are compared with bright-object screening limits before the observations are scheduled. Should unexpectedly bright targets slip through the ground screening process, global and local count rate monitoring in the STIS flight software will initiate protective action. In addition, the tip/tilt capability of the STIS grating wheel will be used to shift the spectral formats of MAMA modes by a small amount periodically to distribute the accumulated illumination more uniformly.

Doppler correction.—The STIS flight software has the capability of performing real-time Doppler compensation for MAMA medium- and high-resolution spectroscopic modes during an exposure to correct for the effects of the spacecraft’s orbital motion. In this process, the flight software adjusts the address to which an event recorded from a MAMA detector is assigned when stored in STIS buffer memory to account for the Doppler shift in the spectral direction. The smallest correction that can be applied corresponds to a shift of 1 MAMA high-resolution pixel, and the correction is updated every minute. Proper operation of the on-board Doppler correction procedure has been verified during SMOV.

Time-tag mode.—STIS has the capability of time-stamping data from the MAMA detectors to an accuracy of 125 μs for event rates below 30,000 counts s^{-1}. The most rigorous flight test of this capability has been the acquisition of time-resolved spectra of the Crab pulsar with the NUV MAMA in mode G230L. The pulse profile derived (integrated over the NUV band) is in excellent agreement with that observed (at higher time resolution) by the *HST* High Speed Photometer in a similar bandpass (Percival et al. 1993). A full analysis of the STIS observation of the Crab pulsar will be presented in a separate publication (Gull et al. 1998).

6. SUMMARY

We have reported here on the results of the first 8 months of on-orbit operation of the STIS. The instrument is performing very well, with all components fully functional. Fundamental instrumental parameters such as sensitivity and resolution are in good agreement with preflight expectations. The results of high S/N performance tests for the MAMA detectors have been extremely encouraging. The only significant anomalies encountered have been the radiation-induced resets to the detector electronics and the unexpectedly high phosphorescent background produced by the NUV MAMA detector window. Scientific observing with the instrument has begun; a number of interesting results are presented elsewhere in this volume. As evidenced by the wide-ranging science program planned by the STIS Guaranteed Time Observers and approved for the General Observer community, we expect the powerful capabilities of STIS to be exploited in studying a diverse array of astrophysical problems in the coming years.

We are grateful to all the people whose efforts over many years made the development of STIS and the execution of the *HST* Second Servicing Mission so successful. The STIS Investigation Definition Team has been funded in response to NASA Announcement of Opportunity OSSA-4-84 through the *Hubble Space Telescope* Project at the Goddard Space Flight Center. This Letter is based on observations with the NASA/ESA *Hubble Space Telescope*, obtained at the Space Telescope Science Institute, which is operated by AURA, Inc., under NASA contract NAS5-26555.

REFERENCES

Baum, S., et al. 1996, STIS Instrument Handbook (Baltimore: STScI)
Biretta, J., et al. 1996, WFPC2 Instrument Handbook (Baltimore: STScI)
Bohlin, R. C. 1996, AJ, 111, 1743
Bohlin, R. C., Colina, L., & Finley, D. S. 1995, AJ, 110, 1316
Bohlin, R. C., Lindler, D. J., & Kaiser, M. E. 1997, STIS ISR 97-07
Bower, G. A., et al. 1998, ApJ, 492, L111
Danks, A. C., et al. 1996, in Science with the *Hubble Space Telescope*—II, ed. P. Benvenuti, F. D. Macchetto, & E. J. Schreier (Baltimore: STScI), 579
Gardner, J. P., et al. 1998, ApJ, 492, L99
Gilliland, R., et al. 1997, STIS Instrument Science Report, in preparation
Gull, T., et al. 1998, in preparation
Heap, S. R., et al. 1998, ApJ, 492, L131

Hutchings, J. B., et al. 1998, ApJ, 492, L115
Jenkins, E. B., et al. 1998, ApJ, 492, L147
Joseph, C. L., et al. 1995, Proc. SPIE, 2551, 248
Kaiser, M. E., Lindler, D. J., & Bohlin, R. C. 1997, in *HST* Calibration Workshop, ed. S. Casertano et al. (Baltimore: STScI), in press
Kasle, D. B., & Morgan, J. S. 1991, Proc. SPIE, 1549, 52
Kimble, R., et al. 1994, Proc. SPIE, 2282, 169
Percival, J., et al. 1993, ApJ, 407, 226
Pian, E., et al. 1998, ApJ, 492, L103
Sahu, K. C., et al. 1998, ApJ, 492, L125
Schroeder, D. J. 1987, Astronomical Optics (San Diego: Academic), 216
Schultz, A. B., et al. 1998, ApJ, 492, L181
Sonneborn, G., et al. 1998, ApJ, 492, L139
Thompson, R. I., Rieke, M., Schneider, G., Hines, D., & Corbin, M. 1998, ApJ, 492, L95
Timothy, J. G. 1994, Proc. SPIE, 2278, 134
Walborn, N. R., et al. 1998, ApJ, 492, L169
Woodgate, B., et al. 1992, in ESO Conf. and Workshop Proc. 44, Science with the Space Telescope, ed. P. Benvenuti & E. Schreier (Munich: ESO), 525
———. 1998, in preparation

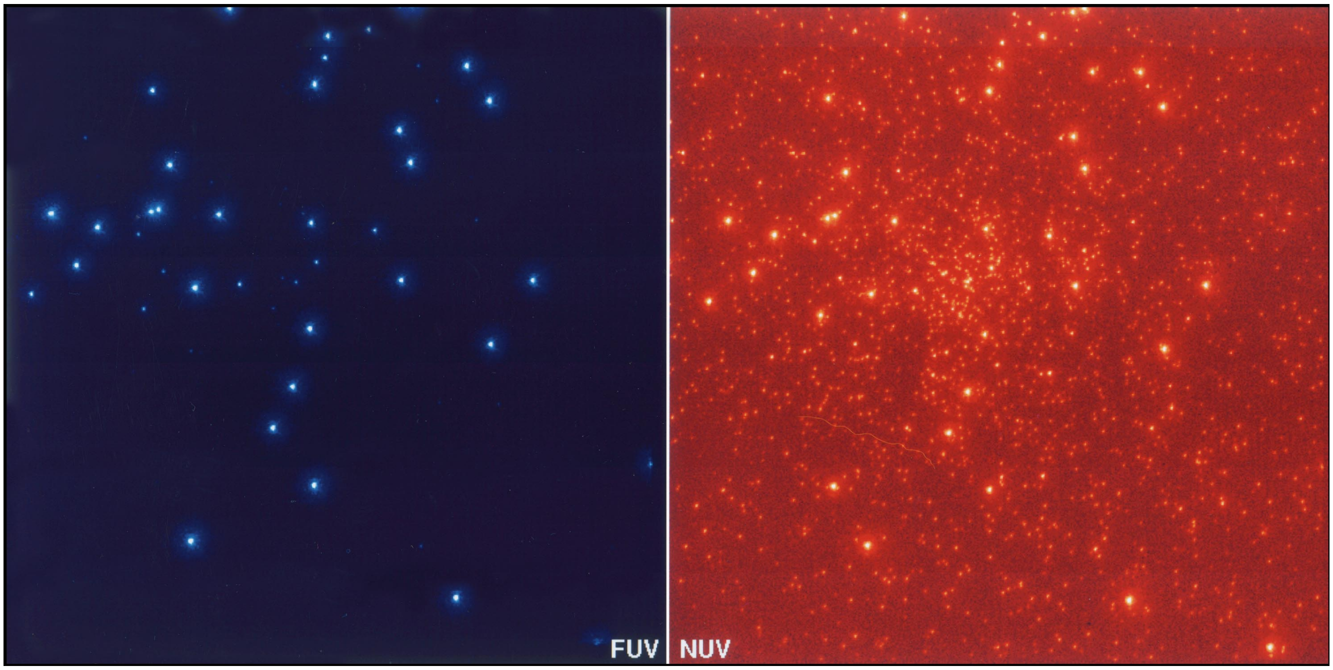

FIG. 3.—UV images of the globular cluster NGC 6681, taken with the STIS MAMA detectors. The raw counts image has been logarithmically scaled in each panel and displayed in false color. *Left panel*: FUV MAMA image through the F25QTZ filter (145–183 nm bandpass, full width at 10% peak), with a 2500 s exposure time. *Right panel*: NUV MAMA image through the F25CN270 filter (257–285 nm bandpass, full width at 10% peak), with a 2600 s exposure time. The images have similar limiting UV magnitudes. Hot horizontal-branch stars stand out dramatically in the FUV image, while cooler, more numerous stellar components of the cluster dominate the NUV image.

KIMBLE et al. (see 492, L90)